GBIR: A NOVEL GAUSSIAN ITERATIVE METHOD FOR MEDICAL IMAGE RECONSTRUCTION

Anonymous authors
Paper under double-blind review

ABSTRACT

Computed Tomography (CT) and Magnetic Resonance Imaging (MRI) are crucial diagnostic tools, but undersampling techniques like Sparse-View CT (SV-CT) and Compressed-Sensing MRI (CS-MRI), aimed at reducing patient exposure and scan time, make image reconstruction more challenging. While deep learning-based reconstruction (DLR) methods have made significant strides, they face limitations in adapting to varying scan geometries and handling diverse patient data, hindering widespread clinical use. In this paper, we propose a novel **G**aussian-**B**ased **I**terative **R**econstruction (**GBIR**) framework that uses learnable Gaussians representations for personalized medical image reconstruction, addressing the shortcomings of DLR methods. GBIR optimizes case-specific parameters in an end-to-end fashion, enabling better generalization and flexibility under sparse measurements. Additionally, we introduce the **M**ulti-**O**rgan Medical Image **RE**construction (**MORE**) dataset, comprising over 70,000 CT and MRI slices across multiple body parts and conditions. Our experiments show that GBIR outperforms state-of-the-art methods in both accuracy and speed, offering a robust solution for personalized medical image reconstruction.

1 INTRODUCTION

Computed Tomography (CT) (Koetzier et al., 2023) and Magnetic Resonance Imaging (MRI) (Harisinghani et al., 2019) are the two most important diagnostic technologies in modern medicine. CT scans use computer processing to reconstruct detailed cross-sectional images from X-rays emitted at various angles and measured as they pass through body tissues. MRI scans use powerful magnets and radio waves to excite hydrogen atoms in the body, generating signals that are detected and processed by a computer to create detailed images of internal structures. Therefore, sophisticated image reconstruction algorithms are essential for both CT and MRI, converting raw data from multiple projections into diagnostic images (Szczykutowicz et al., 2022; Zhu et al., 2018). Modern medical practices use undersampled raw measurements by reducing radiation exposure or scanning time to benefit the health and improve comfort of patients, for example, adopting Sparse-View CT (SV-CT) (Koetzier et al., 2023) and Compressed-Sensing MRI (CS-MRI) (Lustig et al., 2008), as shown in Figure 1. However, these undersampling procedures make the reconstruction process much more challenging, as the raw measurements are insufficient to recover the true 3D conditions within the patient's body.

The scanning process by the machine is usually called the forward process, which acquires the raw measurements from the patient. Conversely, the reconstruction process is called the inverse process that recovers the 3D volume from the raw measurements. The forward process is well studied and can be modeled by mathematical equations, but the inverse process is actually an ill-posed problem with non-unique solutions that is challenging to solve. Traditional methods for medical image reconstruction, such as Filtered Back Projection (FBP) (Bracewell & Riddle, 1967) and Inverse Fast Fourier Transform (IFFT) (Gallagher et al., 2008) for CT and MRI, are incapable of handling the reconstruction problem from sparse measurements. Deep learning-based reconstruction (DLR) methods are leading advancements in medical image reconstruction, offering practical solutions such as SV-CT and CS-MRI for medical diagnosis. While various types of DLR methods exist, such as direct learning methods (Zhu et al., 2018; He et al., 2020), image-domain denoising methods (Jin et al., 2017; Chen et al., 2017), and dual-domain reconstruction methods (Hu et al., 2020), they all share a common principle: employing neural networks to learn the mapping from the measurement domain to the image domain. Nevertheless, SV-CT and CS-MRI have seen limited adoption in

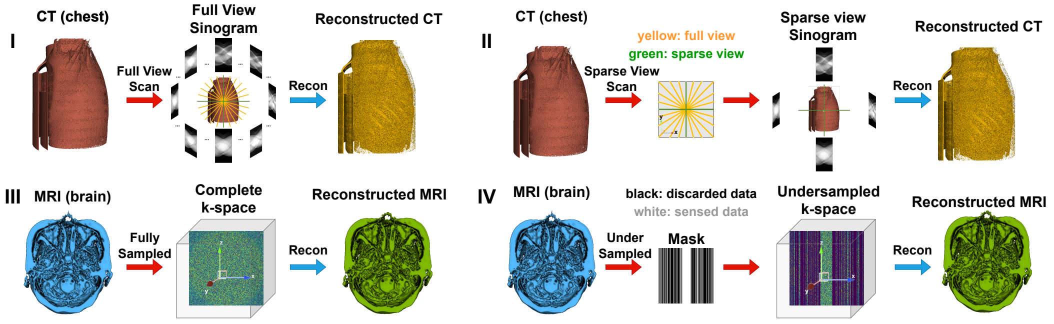

Figure 1: Illustration of medical image reconstruction paradigms. I: Full-View CT scans the patient from multiple angles to acquire complete measurements.; II: Sparse-View CT reduces the number of views to reduce radiation exposure.; III: Complete MRI captures full data sets for high-resolution imaging, ensuring detailed anatomical visualization. IV: Compressed-Sensing MRI reconstructs images from undersampled data, significantly reducing scan time.

clinical practice (Koetzier et al., 2023; Jaspan et al., 2015). The underlying reason is the inherent limitations of neural networks. Firstly, the fixed mapping learned by neural networks poses challenges in adapting to varying scan geometries. For instance, an SV-CT model trained on 60 views cannot be easily extended to 120 or 180 views without undergoing a complete retraining process. Secondly, the effectiveness of neural networks is limited by the diversity of the training data. Variations in patient demographics and medical conditions make it hard to create a comprehensive dataset. Consequently, DLR methods may struggle in clinical practice, as neural networks might fail to reconstruct images for conditions not included in the training data. As noted by Szczykutowicz et al. (2022), future methods should be customized for each individual patient.

Given the numerous inherent limitations of neural networks in medical image reconstruction, we are motivated to take a bold step: abandoning neural networks in favor of a set of learnable isotropic Gaussians to represent the 3D volume to be reconstructed. This idea is inspired by the success of 3D Gaussian Splatting (3DGS) in the field of computer graphics (Kerbl et al., 2023), which uses a set of 3D Gaussians to represent and reconstruct a 3D scene from 2D images. But it is important to note that, unlike 3D scene reconstruction, medical image reconstruction involves supervision signals in the measurement domain rather than the image domain, and the objective is to recover a fixed 3D volume instead of rendering a dynamic 3D scene. Without any Rendering process, in this paper, we propose a novel **G**aussian-**B**ased **I**terative **R**econstruction (**GBIR**) framework that encompasses both high-quality representation and an efficient reconstruction process. GBIR creates a tailored Gaussian representation for each case (patient), with learnable parameters optimized in an end-to-end fashion. This allows for customized medical image reconstruction, overcoming the generalization challenges faced by neural networks, and it also offers flexibility in reconstructing medical images under varying sparse measurement conditions. GBIR requires only the current patient's data for optimization, enabling a "train-as-you-infer" approach.

The main contributions of this paper can be summarized as follows:

- We propose a novel Gaussian-Based Iterative Reconstruction (GBIR) framework. GBIR employs a new reconstruction approach that involves projecting onto the measurement at each iteration, and optimizing the reconstruction based on the loss with the current case's measurement. This method achieves personalized modeling and strong generalization.
- We propose a comprehensive **M**ulti-**O**rgan Medical Image **RE**construction (**MORE**) dataset, which contains over 70,000 slices from 173 patients, covering 15 body parts in CT scans and 5 body parts in MRI scans, with various types of diseases. The dataset has passed the ethical review of the hospital and the local ethics committee and will be released to the public.
- We conduct extensive experiments to evaluate the performance of our proposed method, we compare GBIR with various existing methods on the proposed MORE dataset and other public datasets. The results show GBIR achieves state-of-the-art performance, outperforming other baselines by an obvious margin, and demonstrates superior inference speed.

2 BACKGROUND

Problem Definition The forward process in medical imaging systems (*e.g.*, CT, MRI) can be formulated as follows:

$$y = \mathbf{A}x + n, \tag{1}$$

where x is the 3D volume of the patient, A is the system matrix that models the imaging system, y represents the acquired measurements, and n is the noise. Medical image reconstruction refers to the inverse problem of recovering the 3D volume x from the measurements y. In applications like SV-CT and CS-MRI, the matrix $\mathbf{A}$ is sparse and the measurements y are undersampled, increasing the complexity of the reconstruction process. This inverse problem is inherently ill-posed and non-unique, with the goal being to estimate the most likely 3D volume that corresponds to the given measurements.

A typical approach involves minimizing a loss function that balances the fidelity to the measurements y and the regularization term that imposes prior knowledge about the structure of x. The optimization problem can be written as:

$$\hat{x} = \arg\min_{x} \|\mathbf{A}x - y\|_2^2 + \lambda R(x), \tag{2}$$

where $\hat{x}$ is the estimated 3D volume, $\|\mathbf{A}x - y\|_2^2$ is the fidelity term that measures the discrepancy between the estimated measurements and the acquired measurements, $R(x)$ is the regularization term, which incorporates prior knowledge or assumptions about the image structure, such as smoothness, sparsity, or low-rank characteristics, depending on the specific imaging modality and application. Total variation (TV) (Rudin et al., 1992; Sidky & Pan, 2008) regularization is a common choice for the regularization term in medical image reconstruction, as it preserves the edges and structures of the image while reducing noise. The hyperparameter λ balances the fidelity and regularization terms.

Related Work ***(a) Sparse-View CT***. Classical CT reconstruction methods, such as Filtered Back Projection (FBP) and Iterative Reconstruction (IR), are incapable of handling the Sparse-View CT reconstruction problem. Modern deep learning methods have evolved from convolutional neural networks (CNNs) (Kang et al., 2017; Chen et al., 2017) to generative adversarial networks (GANs) (Yang et al., 2018) and, more recently, to diffusion-based models (Chung et al., 2022; 2023; Xu et al., 2024). Apart from optimization methods like NeRP (Shen et al., 2022), these models typically require large amounts of training data to achieve good performance. ***(b) Compressed-Sensing MRI***. Traditional MRI reconstruction methods rely heavily on the Fourier Transform. However, the performance of Fourier Transform-based reconstruction decreases when the number of sampling points is reduced in Compressed-Sensing MRI. Similar to Sparse-View CT, deep learning methods in this field have evolved from CNNs (Zhu et al., 2018; Hyun et al., 2018) to GANs (Yang et al., 2017; Quan et al., 2018), and finally to diffusion-based models (Chung & Ye, 2022; Chung et al., 2023). A large amount of training data is also required to train these models. ***(c) Relationship with Existing Works.*** We categorize existing medical image reconstruction methods and compare their characteristics in Table 7. Recently, several contemporary works have adapted 3D Gaussian Splatting (3DGS) for CT reconstruction or novel view synthesis (Fu et al., 2024; Lin et al., 2024; Cai et al., 2025; Zha et al., 2024). 3DGR-CAR (Fu et al., 2024) incorporates U-Net (Ronneberger et al., 2015) to predefine Gaussian centers, which are then refined using 3DGS for the final reconstruction process. DIF-Gaussian (Lin et al., 2024) leverages 3D Gaussians to represent feature distributions, facilitating the estimation of attenuation coefficients. X-Gaussian redesigns a radiative Gaussian point cloud model for generating novel views in X-ray imaging applications. R^2-Gaussian (Zha et al., 2024) identifies shortcomings in the use of 3DGS for volumetric reconstruction and introduces an innovative approach to enhance volumetric reconstruction quality.

We emphasize the differences between our proposed method and these approaches. Unlike the above works, our GBIR is not based on 3DGS but introduces a novel Gaussian-based iterative method specifically tailored for medical image reconstruction. The entire process is end-to-end trainable and optimized for medical image reconstruction without any splatting or rendering processes.

3 GAUSSIAN-BASED ITERATIVE RECONSTRUCTION (GBIR)

Figure 2 illustrates our proposed GBIR method, which consists of two parts: **representation** and **reconstruction**. In the following sections, we provide detailed descriptions.

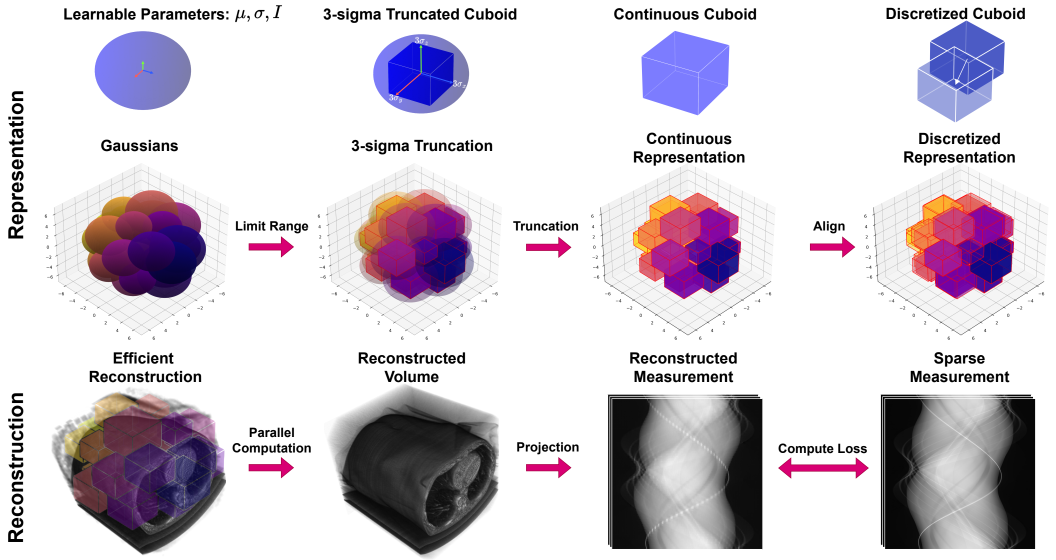

Figure 2: Our GBIR framework for medical image reconstruction. The 3D volume is represented by a set of 3D Gaussians, and the reconstruction process is conducted in an end-to-end manner.

3.1 TRUNCATED THREE-SIGMA GAUSSIAN REPRESENTATION

Basic Formula. We represent the 3D medical volume as the sum of a set of isotropic Gaussians. Each Gaussian function is characterized by its center at a mean value $\boldsymbol{\mu}$ and a covariance $\boldsymbol{\Sigma}$ where $\boldsymbol{\Sigma}$ is a diagonal matrix. We define the Gaussian function as follows:

$$G(\mathbf{x}, \boldsymbol{\mu}, \boldsymbol{\Sigma}) = \exp\left(-\frac{1}{2}(\mathbf{x}-\boldsymbol{\mu})^\top \boldsymbol{\Sigma}^{-1}(\mathbf{x}-\boldsymbol{\mu})\right), \tag{3}$$

where $\mathbf{x} \in \mathbb{R}^d$ represents a 3D point in the scene, exhibiting a bell-shaped curve symmetrically distributed around the mean $\boldsymbol{\mu}$. The spread of this function in the 3D space is determined by the standard deviation $\boldsymbol{\sigma}$.

Naively, we can formulate the reconstruction process of n Gaussians as follows:

$$\mathbf{V} = \sum_{i=1}^{n} G(\mathbf{x}, \boldsymbol{\mu}_i, \boldsymbol{\Sigma}_i) \cdot I_i = \sum_{i=1}^{n} e^{-\frac{1}{2}(\mathbf{x}-\boldsymbol{\mu}_i)^\top \boldsymbol{\Sigma}_i^{-1}(\mathbf{x}-\boldsymbol{\mu}_i)} \cdot I_i = \sum_{i=1}^{n} e^{-\frac{1}{2}D_i^2} \cdot I_i, \tag{4}$$

In this equation, I_i denotes the intensity of the i-th Gaussian. This intensity serves dual purposes: it represents the intensity of the voxel in the volume and also acts as the weight of the Gaussian. The term $(\mathbf{x}-\boldsymbol{\mu})^\top \boldsymbol{\Sigma}^{-1}(\mathbf{x}-\boldsymbol{\mu})$ is recognized as the squared Mahalanobis distance, and we denote it as D_i^2 for the i-th Gaussian for brevity.

However, this formulation is computationally expensive, as it requires the computation of the squared Mahalanobis distance for each voxel in the volume. To address this issue, we introduce a localized Gaussian mapping technique to accelerate the reconstruction process.

Truncated Three-Sigma Gaussian According to the Three-Sigma rule, in Gaussian distribution, the probability of a point falling within three standard deviations of the mean is approximately 99.73% (Appendix B). This implies that the influence of a Gaussian on a voxel diminishes as the distance from the Gaussian center to the voxel increases. By considering only the contributions of Gaussians within a specified proximity of each voxel, we can accelerate the reconstruction process.

Specifically, for each voxel in the 3D volume, we consider a neighborhood $\boldsymbol{\delta}$ around the voxel and compute the contributions of all Gaussians within this neighborhood. The contributions of all Gaussians within their neighborhoods are then added to their corresponding voxels in the volume. This process is repeated for all voxels in the volume, resulting in the final reconstructed 3D volume. The neighborhood around each voxel is centered at the Gaussian center.

Denote the target discretized 3D volume as $\mathbf{V} \in \mathbb{R}^{C\times H\times W}$ where C, H, and W represent the size of the three dimensions, and denote the neighborhood around i-th Gaussian as $\boldsymbol{\delta}_i \in \mathbb{R}^{c\times h\times w\times d}$ where c, h, and w represent the size of the neighborhood, $d = 3$ represents the dimension of 3D coordinates. Note the neighborhood is centered at the Gaussian center $\boldsymbol{\mu}_i$, thus the distance from the points in $\boldsymbol{\delta}_i$ to the center $\boldsymbol{\mu}_i$ is **a constant tensor** for all Gaussians[1], denoted as $\boldsymbol{\delta}' = \boldsymbol{\delta}_i - \boldsymbol{\mu}_i$ with broadcasting applied, where each point $\boldsymbol{p}$ in $\boldsymbol{\delta}_i$ and its corresponding point after transformation $\boldsymbol{p}'$ in $\boldsymbol{\delta}'_i$ satisfies $\boldsymbol{p}' = \boldsymbol{p} - \boldsymbol{\mu}_i$.

Hereby the computation of the squared Mahalanobis distance D_i^2 between the voxel and the Gaussian's mean can be simplified as:

$$D_i^2 = \boldsymbol{\delta}'^{\top}\boldsymbol{\Sigma}_i^{-1}\boldsymbol{\delta}'. \tag{5}$$

Alignment and Differentiability The computation above does not take the discretized grid into account, which is essential for the reconstruction process. The discretized 3D volume $\mathbf{V}$ is composed of integer coordinates, whereas $\boldsymbol{\mu}_i$ is continuous. Direct discretization of $\boldsymbol{\mu}_i$ to the nearest integer for indexing would render the reconstruction process non-differentiable. To address this, we compute each Gaussian's contribution at the discretized grid instead of its continuous position. We denote the $\boldsymbol{\delta}''_i$ as the discretized neighborhood around the Gaussian center. The relationship between $\boldsymbol{\delta}'_i$, $\boldsymbol{\delta}''_i$, and $\boldsymbol{\mu}_i$ is given by:

$$\boldsymbol{\delta}''_i = \boldsymbol{\delta}'_i - (\boldsymbol{\mu}_i - \lfloor \boldsymbol{\mu}_i \rfloor) = \boldsymbol{\delta}'_i - \Delta\boldsymbol{\mu}_i, \tag{6}$$

where we denote $\Delta\boldsymbol{\mu}_i = \boldsymbol{\mu}_i - \lfloor \boldsymbol{\mu}_i \rfloor$ for brevity. Each point $\boldsymbol{p}$ in $\boldsymbol{\delta}'_i$ and its corresponding point after transformation $\boldsymbol{p}'$ in $\boldsymbol{\delta}''_i$ satisfies $\boldsymbol{p}' = \boldsymbol{p} - (\boldsymbol{\mu}_i - \lfloor \boldsymbol{\mu}_i \rfloor)$. From now on, we use subscripts to denote the tensor dimensions to represent the broadcasting operations and tensor-wised operations. For example, Equation 6 will be written as $\boldsymbol{\delta}''_{n,c,h,w,d} = \boldsymbol{\delta}'_{c,h,w,d} - \Delta\boldsymbol{\mu}_{n,1,1,1,d}$. Here, $\boldsymbol{\delta}''_{n,c,h,w,d}$ is the tensor comprised of neighborhoods of all n Gaussians, and $\Delta\boldsymbol{\mu}_{n,1,1,1,d}$ implicitly denotes the expansion of $\Delta\boldsymbol{\mu}_{n,d}$ to identical dimensions for element-wise subtraction.

3.2 EFFICIENT RECONSTRUCTION

On the discretized 3D grid, the computation of the squared Mahalanobis distance tensor $D^2_{n,c,h,w}$ can be formulated as the Einstein summation:

$$D^2_{n,c,h,w} = \sum_d \boldsymbol{\delta}''^{\top}_{n,c,h,w,d}\boldsymbol{\Sigma}^{-1}_{n,d,d}\boldsymbol{\delta}''_{n,c,h,w,d}. \tag{7}$$

By combining Equations 6 and 7, we decompose the large Einstein summation above into the sum of four smaller Einstein summations:

$$\begin{aligned} D^2_{n,c,h,w} = &\sum_d \boldsymbol{\delta}'_{c,h,w,d}\boldsymbol{\Sigma}^{-1}_{n,d,d}\boldsymbol{\delta}'_{c,h,w,d} - \sum_d \boldsymbol{\delta}'_{c,h,w,d}\boldsymbol{\Sigma}^{-1}_{n,d,d}\Delta\boldsymbol{\mu}_{n,1,1,d} \\ &- \sum_d \Delta\boldsymbol{\mu}_{n,1,1,d}\boldsymbol{\Sigma}^{-1}_{n,d,d}\boldsymbol{\delta}'_{c,h,w,d} + \sum_d \Delta\boldsymbol{\mu}_{n,1,1,d}\boldsymbol{\Sigma}^{-1}_{n,d,d}\,\Delta\boldsymbol{\mu}_{n,1,1,d}. \end{aligned} \tag{8}$$

Then we can compute the contributions of all Gaussians, denoted as $\Gamma_{n,c,h,w}$, as the following:

$$\Gamma_{n,c,h,w} = e^{-\frac{1}{2}D^2_{n,c,h,w}} \cdot I_n. \tag{9}$$

Note that $\Gamma_{n,c,h,w}$ is the contributions of all Gaussians within their neighborhoods, and the final step is to add up all the contributions to their corresponding voxels in the volume. A direct way is to loop over each Gaussian and add its contribution to the volume as $\mathbf{V}[\boldsymbol{\delta}_i] \leftarrow \mathbf{V}[\boldsymbol{\delta}_i] + \Gamma_i$. For acceleration, we use the parallel accumulation operation to compute the contributions of all Gaussians within their neighborhoods in parallel.

$$\mathbf{V}_{c,h,w} = \text{parallel\_accumulate}(\Gamma_{n,c,h,w}, \boldsymbol{\delta}_{n,c,h,w,d}). \tag{10}$$

---

[1] The shape of the Gaussian function remains invariant under translation; shifting the parameter μ changes the peak's location but does not alter the overall shape of the function.

3.3 OPTIMIZATION IN MEASUREMENT DOMAIN

After the 3D volume is reconstructed, we transform the 3D volume to the measurement domain and directly optimize it under the supervision of the current patient's measurement. The transformation $\mathcal{F}$ from the 3D volume to the measurement domain is achieved through the Radon transform for CT and Fourier transform for MRI[2].

$$\hat{\mathbf{M}} = \mathcal{F}(\mathbf{V}) = \begin{cases} Radon(\mathbf{V}), & \text{for CT} \\ Fourier(\mathbf{V}), & \text{for MRI} \end{cases} \tag{11}$$

where $\hat{\mathbf{M}}$ is the estimated measurement. Then the optimization problem becomes to minimize the discrepancy between the estimated measurement $\hat{\mathbf{M}}$ and the sparse measurement $\mathbf{M}$. We penalize the discrepancy in the measurement domain by L_1 norm and Structure Similarity Index (SSIM). Besides, we add a total variation (TV) regularization term to the 3D volume to preserve the structure of the volume. The optimization problem can be formulated as:

$$\min_{\mathbf{V}} \lambda_1 \left\| \hat{\mathbf{M}} - \mathbf{M} \right\|_1 + \lambda_2 (1 - \text{SSIM}(\hat{\mathbf{M}}, \mathbf{M})) + \lambda_3 \text{TV}(\mathbf{V}), \tag{12}$$

where $\lambda_1 = 1$, $\lambda_2 = 500$, and $\lambda_3 = 500$ are hyperparameters to balance the three terms. For the MRI reconstruction, the measurement M and the estimated measurement $\hat{M}$ are complex-valued, and we compute the loss separately for the real and imaginary parts and sum them up. Iteratively, we update the parameters of the Gaussians to minimize the objective function. The optimization process is conducted in an end-to-end manner, and the final 3D volume is obtained after convergence.

4 MULTI-ORGAN MEDICAL IMAGE RECONSTRUCTION DATASET (MORE)

Existing datasets usually focus on a single body part or disease, which substantially hinders a more thorough and comprehensive assessment of current research on medical image reconstruction. Advanced methods including (Chung et al., 2023; Xu et al., 2024; Yang et al., 2022; Xia et al., 2022) usually evaluate on a single body part, such as only abdomen part in AAPM-Mayo LDCT Challenge Dataset (Moen et al., 2021), or only brain part in BRATS (Menze et al., 2014) dataset. It is difficult to conclude the effectiveness of a method based solely on the results of a single body part, and its generalization ability remains to be verified. To address this limitation, we propose the **M**ulti-**O**rgan Medical Image **RE**construction (**MORE**) dataset, which has the following characteristics:

- It incorporates both CT and MRI data types, and a diverse set of body parts. To be specific, MORE contains over 65,755 CT slices and 7,498 MRI slices from 173 patients, covering 15 body parts in CT scans and 5 body parts in MRI scans. Table 1 presents a detailed comparison of MORE with existing medical image reconstruction datasets.
- MORE exhibits a rational distribution of demographics and diseases. To be specific, MORE involves a total of 173 patients and 189 examinations. Some patients underwent multiple examinations, resulting in 135 CT scans and 54 MRI scans. The median age of the participants was 52 years, ranging from 7 to 85 years. The age distribution is as follows: 0-20 years (5.4%), 21-40 years (29.5%), 41-60 years (37.2%), 61-80 years (24.0%), 81-100 years (3.9%). The gender distribution was 59.7% male and 40.3% female. MORE contains 25 types of diseases in CT and 17 types of diseases in MRI, respectively. We show the specific distribution of the CT and MRI scans in Figure 3 and Figure 4, and provide some samples in Figure 6 for visualization.
- MORE has been approved by the ethics committee of corresponding hospital, and the approval number also has been obtained[3]. All DICOM data has been anonymized by RSNA clinical trial processor to protect patient privacy and comply with the Helsinki declaration. We will release the dataset for public availability.

  Currently, MORE dataset provides DICOM images and does not include the original raw measurements. This aligns with common practices in medical image reconstruction research as demonstrated by several advanced methods (Yang et al., 2022; Chung et al., 2023; Xu et al., 2024), which often rely on simulated measurements generated from image slices. In the experiments, we simulate measurements by applying the Radon transform for CT data and the Fourier transform for MRI data following previous research (Xu et al., 2024; Chung et al., 2023).

---

[2] In this paper, we only reconstruct the magnitude of the MRI image, which is real-valued.

[3] Due to the double-blind policy, the information of the hospital will be disclosed after the review process.

Table 1: Comparison of MORE with existing medical image reconstruction datasets. ‘New Source’ means whether the dataset is collected from new source or not.

Dataset	#Body Parts	#Images	New Source
MORE	**15** (CT) / **5** (MRI)	65,755 CT, 7,498 MRI	✓
AAPM-Mayo LDCT (Moen et al., 2021)	3 (chest, abdomen, head)	25,141 CT	✓
LoDoPaB-CT (Leuschner et al., 2021)	1 (chest)	46,573 CT	×
Covidx-CT (Gunraj et al., 2020)	1 (chest)	104,009 CT	×
LIDC/IDRI (Armato III et al., 2011)	1 (chest)	1,018 CT	✓
FUMPE (Masoudi et al., 2018)	1 (chest)	8,792 CT	✓
JSRT (Shiraishi et al., 2000)	1 (chest)	247 CT	✓
Fast MRI (Knoll et al., 2020)	3 (knee, brain, prostate)	167,375 MRI	✓
SKM-TEA (Desai et al., 2022)	1 (knee)	25,000 MRI	✓
Calgary-Campinas-359 (Souza et al., 2018)	1 (brain)	42,752 MRI	✓
BraTS (Menze et al., 2014)	1 (brain)	57,195 MRI	✓

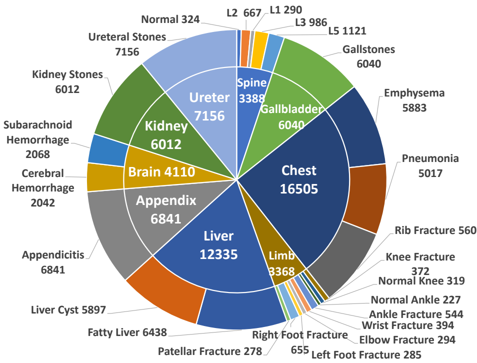

Figure 3: Data distribution of MORE CT part, containing 15 organs and 25 disease types.

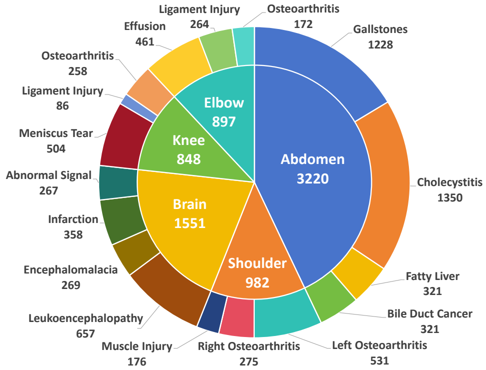

Figure 4: Data distribution of MORE MRI part, containing 5 organs and 17 disease types.

5 EXPERIMENTS

In this section, we extensively evaluate and benchmark various types of methods on both public widely used datasets and our newly proposed MORE dataset.

5.1 EXPERIMENTAL SETTINGS

Datasets We extensively benchmark various methods on both public widely used datasets and our newly proposed MORE dataset. For the public dataset, we use the widely-used AAPM-Mayo LDCT Challenge Dataset (Moen et al., 2021) for CT reconstruction, and the BRATS dataset (Menze et al., 2014) for MRI reconstruction with those learning-based methods pretrained on the fastMRI dataset (Knoll et al., 2020) following the setting of our baseline method DiffusionMBIR (Chung et al., 2023). We simulate the sparse-view CT reconstruction of fan-beam geometry with 60, 90, 120, and 180 views, and the MRI reconstruction by 1D uniform distribution with an acceleration factor of 2 to subsample the k-space data.

Evaluation Metrics We follow the standard practice in medical image reconstruction (Chung et al., 2023; Xu et al., 2024; Chen et al., 2017) to evaluate the performance of different methods using the Peak Signal-to-Noise Ratio (PSNR) (Hore & Ziou, 2010) and the Structural Similarity Index (SSIM) (Wang et al., 2004). The detailed definitions of PSNR and SSIM are provided in Appendix A.

Compared Methods We compare our proposde GBIR method with different types of baselines which covering representative methods to state-of-the-art methods. We choose traditional methods FBP (Bracewell & Riddle, 1967) and IFFT (Gallagher et al., 2008) that widely used in clinical practice, early DLR methods REDCNN (Chen et al., 2017), AUTOMAP (Zhu et al., 2018), and the 3D Scene-based method NeRP (Shen et al., 2022) that implicitly learn the prior from the data, and

Table 2: Efficiency of different methods in terms of time and GPU memory consumption during training and inference.'Train' and 'Inference' are denoted as 'T.' and 'Inf.', respectively. MCG and DiffusionMBIR share the same score function and thus have the same training time and memory consumption.

Method	T. Time (min)	T. Mem (MiB)	Inf. Time (min)	Inf. Mem (MiB)
RED-CNN (Chen et al., 2017)	221	4857	2.4	1665
AUTOMAP (Zhu et al., 2018)	33.4	9.75	≈ 0.2	49140
Score-MRI (Chung & Ye, 2022)	9833	6143	1941	16685
MCG (Chung et al., 2022)	10342	7103	3290	7392
DiffusionMBIR (Chung et al., 2023)	10342	7103	1983	16673
SWORD (Xu et al., 2024)	3017	16580	5094	3051
NeRP (Shen et al., 2022)	0	0	1121	44927
GBIR (Ours)	0	0	464	34126

Table 3: SV-CT reconstruction on AAPM-Mayo LDCT dataset. Best in **Bold.**

Method	Extra Data	180-view		120-view		90-view		60-view	
		PSNR	SSIM	PSNR	SSIM	PSNR	SSIM	PSNR	SSIM
FBPConvNet (Jin et al., 2017)	✓	42.23	0.988	39.45	0.983	37.11	0.976	35.63	0.966
U-Net (TRPMS 18) (Lee et al., 2018)	✓	38.37	0.985	35.58	0.977	30.09	0.947	28.83	0.937
PLANet (ACM'MM 22) (Yang et al., 2022)	✓	42.76	0.965	41.67	0.962	40.99	0.957	38.97	0.941
DDPM (Xia et al., 2022)	✓	40.95	0.985	37.90	0.976	35.15	0.963	32.04	0.934
MCG (Chung et al., 2022)	✓	40.42	0.969	39.57	0.960	38.02	0.935	37.17	0.921
DiffusionMBIR (Chung et al., 2023)	✓	41.78	0.990	40.83	0.964	39.98	0.942	38.67	0.932
GMSD (TRPMS 23) (Guan et al., 2023)	✓	41.44	0.988	39.41	0.981	37.25	0.974	34.31	0.958
SWORD (Xu et al., 2024)	✓	45.08	0.994	42.49	0.990	41.27	0.986	38.49	0.978
FBP (Bracewell & Riddle, 1967)	×	31.69	0.882	28.30	0.787	26.20	0.701	23.18	0.595
GBIR (Ours)	×	**46.39**	**0.995**	**45.24**	**0.994**	**43.21**	**0.991**	**40.17**	**0.985**

most advanced diffusion-based DLR methods DiffusionMBIR (Chung et al., 2023), MCG (Chung et al., 2022), score-mri (Chung & Ye, 2022), SWORD (Xu et al., 2024).

Experimental Settings As shown in Table 7, most methods, particularly DLR methods, require the entire training dataset to learn parameters. We mark these methods as requiring 'Extra Data'. For other optimization-based methods, including FBP (Bracewell & Riddle, 1967), IFFT (Gallagher et al., 2008), NeRP (Shen et al., 2022), and our GBIR, we directly evaluate the performance on the test set without using any training data. All experiments are conducted on an Ubuntu server equipped with an NVIDIA RTX 6000 Ada Generation GPU with 48 GiB of memory.

Hyperparameter Setting For our proposed GBIR framework, we initialize the number of Gaussians to 150. We use the Adam optimizer with a learning rate of 3e-4 and decay to 3e-5 at the end of training. For 60-view, 90-view, 120-view, and 180-view SV-CT, we set the training iteration to 5K, 6K, and 7K, and 10K, respectively. For the CS-MRI, we set the training iteration to 3K.

5.2 SPARSE-VIEW CT ON AAPM-MAYO LDCT DATASET

AAPM-Mayo LDCT Challenge Dataset is widely used for Sparse-View CT reconstruction, and we follow the latest state-of-the-art method SWORD (Xu et al., 2024) to conduct the evaluation with 60-view, 90-view, 120-view, and 180-view, which is also a common setting adopted (Guan et al., 2023; Yang et al., 2022). The results are shown in Table 3. Our proposed GBIR outperforms all the compared methods in terms of PSNR and SSIM without bells and whistles.

5.3 COMPRESSED-SENSING MRI ON BRATS DATASET

We evaluate the performance of different methods on the BRATS dataset for CS-MRI reconstruction following the setting in Chung et al. (2023); Chung & Ye (2022). The result of DuDoRNet (Lahiri

Table 4: CS-MRI reconstruction on BRATS dataset. Best in **Bold.**

Method	Extra Data	Axial		Coronal		Sagittal	
		PSNR	SSIM	PSNR	SSIM	PSNR	SSIM
RED-CNN (Chen et al., 2017)	✓	33.23	0.920	29.11	0.916	28.91	0.910
Unet (Lee et al., 2018)	✓	37.15	0.929	31.56	0.899	30.90	0.816
DuDoRNet (Lahiri et al., 2023)	✓	39.78	0.974	33.56	0.927	33.48	0.927
AUTOMAP (Zhu et al., 2018)	✓	31.11	0.913	30.96	0.905	29.39	0.895
ScoreMRI (Chung & Ye, 2022)	✓	40.38	0.968	33.97	0.925	34.02	0.928
DiffusionMBIR (Chung et al., 2023)	✓	**41.49**	**0.974**	37.36	0.942	37.18	0.953
IFFT (Gallagher et al., 2008)	×	32.15	0.914	31.80	0.911	31.44	0.910
GBIR (Ours)	×	40.40	0.973	**39.64**	**0.969**	**39.45**	**0.968**

Table 5: Effectiveness of Three-Sigma Gaussian Truncation.

	PSNR	SSIM	Inference Time (h)	Space Consumption (GiB)
$11 \times 11 \times 11$	44.64	0.989	5.88	32.24
$13 \times 13 \times 13$	45.38	0.991	8.10	38.22
$15 \times 15 \times 15$	46.05	0.993	11.46	47.53
$Three - Sigma$	**46.39**	**0.995**	7.73	33.32

et al., 2023) is sourced from Chung et al. (2023). Different from CT, MRI scans are usually conducted in three different directions, including axial, coronal, and sagittal. The results are shown in Table 4. Our proposed GBIR achieves the best performance in coronal and sagittal views, and the second-best performance in the axial view, which is only slightly lower than the best method. Besides, GBIR shows a more balanced performance across different views compared to other methods.

5.4 BENCHMARK AND FINDINGS ON MORE DATASET

We benchmark the performance of different methods on the newly proposed MORE dataset, which contains a wide range of body parts and diseases. Our benchmark include 15 body parts and 25 diseases for CT scans (Table 9 to Table 23), and 5 body parts and 17 diseases for MRI scans (Table 24 to Table 28). To the best of our knowledge, this is the first time that such a comprehensive dataset is used for evaluating medical image reconstruction methods. More than comparing the performance, we also provide some insights and findings from the benchmark on the MORE dataset.

Optimization-based methods are more robust to the influence of data.: We observe that optimization-based methods, including FBP (Bracewell & Riddle, 1967), IFFT (Gallagher et al., 2008), NeRP (Shen et al., 2022), and our GBIR, show consistent performance across different body parts and diseases. In contrast, learning-based methods, such as REDCNN (Chen et al., 2017), AUTOMAP (Zhu et al., 2018), and score-mri (Chung & Ye, 2022), show a more significant performance variation across different body parts and diseases. This indicates that optimization-based methods are more robust to the influence of data, while learning-based methods are more sensitive to the data distribution.

A comprehensive dataset helps improve the generalization ability for learning-based methods: Table 8 and Table 23 both are evaluated on the subarachnoid hemorrhage disease, but their training data are different. The former is trained on the AAPM-Mayo LDCT dataset, while the latter is trained on the MORE dataset. We observe that the learning-based methods, including REDCNN (Chen et al., 2017), AUTOMAP (Zhu et al., 2018), and score-mri (Chung & Ye, 2022), show better performance when trained on the MORE dataset compared to the AAPM-Mayo LDCT dataset. This indicates that a comprehensive dataset with diverse body parts and diseases can help improve the generalization ability of learning-based methods.

Significant performance variation across different body parts: We observe that the performance of different methods varies significantly across different body parts and diseases. Figure 7 and Figure 8 show the distribution of PSNR and SSIM across different body parts and diseases for CT and MRI scans, respectively. We observe that the performance of different methods varies significantly across different body parts and diseases. For example, the performance of RED-CNN is considerably

Table 6: Effectiveness of Efficient Reconstruction.

	Direct Reconstruction	Non-Parallel Reconstruction	Efficient Reconstruction
Rendering Time (s)	1.03-1.12	0.98-1.09	0.09-0.12
Space Consumption (GiB)	47.98	33.32	33.32

lower on the **Emphysema** part compared to the **Ureteral Calculi** part. It is important to evaluate the performance on a diverse dataset with multiple organs to ensure the robustness of the method.

Furthermore, our GBIR method shows the best performance across different body parts and diseases on the MORE dataset, which demonstrates the effectiveness and robustness of our proposed method.

5.5 ABLATION STUDY AND EFFICIENCY ANALYSIS

To avoid confusion with the training time, inference time, and rendering time, here the training time refers to the time consumed for training the neural network for DLR methods, while the inference time refers to the time consumed for reconstructing the volume. Thus, NeRP (Shen et al., 2022) and our GBIR do not have training time, as they do not require any training data. The rendering time refers to the time consumed for reconstructing the volume from the Gaussians.

Computational Efficiency We provide an efficiency analysis of different methods in terms of training time, GPU memory consumption, inference time, and GPU memory consumption. The results are shown in Table 2. Our proposed GBIR achieves the best efficiency in terms of training time and GPU memory consumption, as it does not require any training data. In contrast, learning-based methods, such as RED-CNN (Chen et al., 2017), score-mri (Chung & Ye, 2022), and MCG (Chung et al., 2022), require a large amount of training data and thus consume more training time and GPU memory. For inference time and GPU memory consumption, our proposed GBIR achieves better efficiency than the advanced diffusion-based methods and NeRP, which is essential for real-time applications in clinical practice.

Effect of Three-Sigma Truncation We evaluate the effect of Three-Sigma truncation in the GBIR framework on AAPM-Mayo LDCT dataset 180-view SV-CT. We substitute the Three-Sigma truncation with different size of cuboid box, including $11 \times 11 \times 11$, $13 \times 13 \times 13$, and $15 \times 15 \times 15$. The results are shown in Table 5.

Effect of Efficient Reconstruction In Table 6, we compare the rendering time and space consumption of direct reconstruction, non-parallel reconstruction, and efficient reconstruction. Specifically, direct reconstruction refers to the reconstruction with formula 7, non-parallel reconstruction refers to the reconstruction process without parallel computation.

6 DISCUSSION

Limitations It should be noted that although our proposed GBIR is faster than the advanced methods, it is still slower than the traditional DLR methods. In Table 2, the inference time of RED-CNN and AUTOMAP is much shorter than all other advanced methods. Nevertheless, their performance is significantly lower. This trade-off between speed and performance is a common challenge in medical image reconstruction, and it remains an open problem for future research.

Visualization We include a visualization of the reconstruction process in Appendix 5 to provide a better understanding of the reconstruction process of our proposed GBIR method. Iteration by iteration, the reconstruction becomes clearer and more detailed. We also provide histograms of PSNR on the MORE dataset of 60-view SV-CT and axial CS-MRI in Figure 7 and Figure 8, respectively. The histograms show the distribution of PSNR across different body parts and diseases, providing insights into the performance of different methods on the MORE dataset.

Conclusion In this paper, we present a novel Gaussian-based image reconstruction method, GBIR, which achieves state-of-the-art performance on both public widely used datasets and our newly proposed MORE dataset. Our proposed method is efficient and robust, making it suitable for tailored reconstruction of different body parts and diseases. We also provide a comprehensive benchmark on the MORE dataset, which includes a wide range of body parts and diseases, to facilitate further research in medical image reconstruction.

ETHICS STATEMENT

We make the following ethical considerations in our work:

- Our proposed MORE dataset has been collected with the approval of the hospital ethics committee.
- All information that could potentially identify patients has been removed from the dataset to ensure patient privacy.
- All other datasets used in our work are publicly available and have been used in accordance with the terms of use.
- We have followed the standard practice in medical image reconstruction and have conducted our experiments in a responsible and ethical manner.
- We have provided a detailed description of our methods and results to ensure transparency and reproducibility.
- We will make our code and data publicly available to facilitate further research and ensure transparency.

REPRODUCIBILITY STATEMENT

We provide the following information to facilitate the reproducibility of our work:

- We include the metadata of the MORE dataset in the supplementary material for reference.
- We have provided the detailed experimental results and evaluation metrics in the paper to ensure transparency and reproducibility.
- After the double-blind review process, we will make our code and data publicly available to facilitate further research and ensure transparency.

REFERENCES

Samuel G Armato III, Geoffrey McLennan, Luc Bidaut, Michael F McNitt-Gray, Charles R Meyer, Anthony P Reeves, Binsheng Zhao, Denise R Aberle, Claudia I Henschke, Eric A Hoffman, et al. The lung image database consortium (lidc) and image database resource initiative (idri): a completed reference database of lung nodules on ct scans. *Medical physics*, 38(2):915–931, 2011.

Ronald Newbold Bracewell and ACf Riddle. Inversion of fan-beam scans in radio astronomy. *Astrophysical Journal, vol. 150, p. 427*, 150:427, 1967.

Yuanhao Cai, Yixun Liang, Jiahao Wang, Angtian Wang, Yulun Zhang, Xiaokang Yang, Zongwei Zhou, and Alan Yuille. Radiative gaussian splatting for efficient x-ray novel view synthesis. In *European Conference on Computer Vision*, pp. 283–299. Springer, 2025.

Hu Chen, Yi Zhang, Mannudeep K Kalra, Feng Lin, Yang Chen, Peixi Liao, Jiliu Zhou, and Ge Wang. Low-dose ct with a residual encoder-decoder convolutional neural network. *IEEE transactions on medical imaging*, 36(12):2524–2535, 2017.

Hyungjin Chung and Jong Chul Ye. Score-based diffusion models for accelerated mri. *Medical image analysis*, 80:102479, 2022.

Hyungjin Chung, Byeongsu Sim, Dohoon Ryu, and Jong Chul Ye. Improving diffusion models for inverse problems using manifold constraints. *Advances in Neural Information Processing Systems*, 35:25683–25696, 2022.

Hyungjin Chung, Dohoon Ryu, Michael T Mccann, Marc L Klasky, and Jong Chul Ye. Solving 3d inverse problems using pre-trained 2d diffusion models. ieee. In *CVF Conference on Computer Vision and Pattern Recognition*, volume 1, pp. 6, 2023.

Arjun D Desai, Andrew M Schmidt, Elka B Rubin, Christopher M Sandino, Marianne S Black, Valentina Mazzoli, Kathryn J Stevens, Robert Boutin, Christopher Ré, Garry E Gold, et al. Skm-tea: A dataset for accelerated mri reconstruction with dense image labels for quantitative clinical evaluation. *arXiv preprint arXiv:2203.06823*, 2022.

Xueming Fu, Yingtai Li, Fenghe Tang, Jun Li, Mingyue Zhao, Gao-Jun Teng, and S Kevin Zhou. 3dgr-car: Coronary artery reconstruction from ultra-sparse 2d x-ray views with a 3d gaussians representation. In *International Conference on Medical Image Computing and Computer-Assisted Intervention*, pp. 14–24. Springer, 2024.

Thomas A Gallagher, Alexander J Nemeth, and Lotfi Hacein-Bey. An introduction to the fourier transform: relationship to mri. *American journal of roentgenology*, 190(5):1396–1405, 2008.

Bing Guan, Cailian Yang, Liu Zhang, Shanzhou Niu, Minghui Zhang, Yuhao Wang, Weiwen Wu, and Qiegen Liu. Generative modeling in sinogram domain for sparse-view ct reconstruction. *IEEE Transactions on Radiation and Plasma Medical Sciences*, 2023.

Hayden Gunraj, Linda Wang, and Alexander Wong. Covidnet-ct: A tailored deep convolutional neural network design for detection of covid-19 cases from chest ct images. *Frontiers in medicine*, 7:608525, 2020.

Mukesh G Harisinghani, Aileen O'Shea, and Ralph Weissleder. Advances in clinical mri technology. *Science Translational Medicine*, 11(523):eaba2591, 2019.

Ji He, Yongbo Wang, and Jianhua Ma. Radon inversion via deep learning. *IEEE transactions on medical imaging*, 39(6):2076–2087, 2020.

Alain Hore and Djemel Ziou. Image quality metrics: Psnr vs. ssim. In *2010 20th international conference on pattern recognition*, pp. 2366–2369. IEEE, 2010.

Dianlin Hu, Jin Liu, Tianling Lv, Qianlong Zhao, Yikun Zhang, Guotao Quan, Juan Feng, Yang Chen, and Limin Luo. Hybrid-domain neural network processing for sparse-view ct reconstruction. *IEEE Transactions on Radiation and Plasma Medical Sciences*, 5(1):88–98, 2020.

Chang Min Hyun, Hwa Pyung Kim, Sung Min Lee, Sungchul Lee, and Jin Keun Seo. Deep learning for undersampled mri reconstruction. *Physics in Medicine & Biology*, 63(13):135007, 2018.

Oren N Jaspan, Roman Fleysher, and Michael L Lipton. Compressed sensing mri: a review of the clinical literature. *The British journal of radiology*, 88(1056):20150487, 2015.

Kyong Hwan Jin, Michael T McCann, Emmanuel Froustey, and Michael Unser. Deep convolutional neural network for inverse problems in imaging. *IEEE transactions on image processing*, 26(9): 4509–4522, 2017.

Eunhee Kang, Junhong Min, and Jong Chul Ye. A deep convolutional neural network using directional wavelets for low-dose x-ray ct reconstruction. *Medical physics*, 44(10):e360–e375, 2017.

Bernhard Kerbl, Georgios Kopanas, Thomas Leimkühler, and George Drettakis. 3d gaussian splatting for real-time radiance field rendering. *ACM Transactions on Graphics*, 42(4):1–14, 2023.

Florian Knoll, Jure Zbontar, Anuroop Sriram, Matthew J Muckley, Mary Bruno, Aaron Defazio, Marc Parente, Krzysztof J Geras, Joe Katsnelson, Hersh Chandarana, et al. fastmri: A publicly available raw k-space and dicom dataset of knee images for accelerated mr image reconstruction using machine learning. *Radiology: Artificial Intelligence*, 2(1):e190007, 2020.

Lennart Koetzier, Domenico Mastrodicasa, Timothy Szczykutowicz, Niels Werf, Adam Wang, Veit Sandfort, Aart van der Molen, Dominik Fleischmann, and Martin Willemink. Deep learning image reconstruction for ct: Technical principles and clinical prospects. *Radiology*, 306, 01 2023. doi: 10.1148/radiol.221257.

Anish Lahiri, Gabriel Maliakal, Marc L Klasky, Jeffrey A Fessler, and Saiprasad Ravishankar. Sparse-view cone beam ct reconstruction using data-consistent supervised and adversarial learning from scarce training data. *IEEE Transactions on Computational Imaging*, 9:13–28, 2023.

Hoyeon Lee, Jongha Lee, Hyeongseok Kim, Byungchul Cho, and Seungryong Cho. Deep-neural-network-based sinogram synthesis for sparse-view ct image reconstruction. *IEEE Transactions on Radiation and Plasma Medical Sciences*, 3(2):109–119, 2018.

Johannes Leuschner, Maximilian Schmidt, Daniel Otero Baguer, and Peter Maass. Lodopab-ct, a benchmark dataset for low-dose computed tomography reconstruction. *Scientific Data*, 8(1):109, 2021.

Yiqun Lin, Hualiang Wang, Jixiang Chen, and Xiaomeng Li. Learning 3d gaussians for extremely sparse-view cone-beam ct reconstruction. *arXiv preprint arXiv:2407.01090*, 2024.

Michael Lustig, David L Donoho, Juan M Santos, and John M Pauly. Compressed sensing mri. *IEEE signal processing magazine*, 25(2):72–82, 2008.

Mojtaba Masoudi, Hamid-Reza Pourreza, Mahdi Saadatmand-Tarzjan, Noushin Eftekhari, Fateme Shafiee Zargar, and Masoud Pezeshki Rad. A new dataset of computed-tomography angiography images for computer-aided detection of pulmonary embolism. *Scientific data*, 5(1): 1–9, 2018.

Bjoern H Menze, Andras Jakab, Stefan Bauer, Jayashree Kalpathy-Cramer, Keyvan Farahani, Justin Kirby, Yuliya Burren, Nicole Porz, Johannes Slotboom, Roland Wiest, et al. The multimodal brain tumor image segmentation benchmark (brats). *IEEE transactions on medical imaging*, 34(10): 1993–2024, 2014.

Taylor R Moen, Baiyu Chen, David R Holmes III, Xinhui Duan, Zhicong Yu, Lifeng Yu, Shuai Leng, Joel G Fletcher, and Cynthia H McCollough. Low-dose ct image and projection dataset. *Medical physics*, 48(2):902–911, 2021.

Tran Minh Quan, Thanh Nguyen-Duc, and Won-Ki Jeong. Compressed sensing mri reconstruction using a generative adversarial network with a cyclic loss. *IEEE transactions on medical imaging*, 37(6):1488–1497, 2018.

Olaf Ronneberger, Philipp Fischer, and Thomas Brox. U-net: Convolutional networks for biomedical image segmentation. In *Medical image computing and computer-assisted intervention–MICCAI 2015: 18th international conference, Munich, Germany, October 5-9, 2015, proceedings, part III 18*, pp. 234–241. Springer, 2015.

Leonid I Rudin, Stanley Osher, and Emad Fatemi. Nonlinear total variation based noise removal algorithms. *Physica D: nonlinear phenomena*, 60(1-4):259–268, 1992.

Liyue Shen, John Pauly, and Lei Xing. Nerp: implicit neural representation learning with prior embedding for sparsely sampled image reconstruction. *IEEE Transactions on Neural Networks and Learning Systems*, 2022.

Junji Shiraishi, Shigehiko Katsuragawa, Junpei Ikezoe, Tsuneo Matsumoto, Takeshi Kobayashi, Ken-ichi Komatsu, Mitate Matsui, Hiroshi Fujita, Yoshie Kodera, and Kunio Doi. Development of a digital image database for chest radiographs with and without a lung nodule: receiver operating characteristic analysis of radiologists' detection of pulmonary nodules. *American journal of roentgenology*, 174(1):71–74, 2000.

Emil Y Sidky and Xiaochuan Pan. Image reconstruction in circular cone-beam computed tomography by constrained, total-variation minimization. *Physics in Medicine & Biology*, 53(17):4777, 2008.

Roberto Souza, Oeslle Lucena, Julia Garrafa, David Gobbi, Marina Saluzzi, Simone Appenzeller, Letícia Rittner, Richard Frayne, and Roberto Lotufo. An open, multi-vendor, multi-field-strength brain mr dataset and analysis of publicly available skull stripping methods agreement. *NeuroImage*, 170:482–494, 2018.

Timothy P Szczykutowicz, Giuseppe V Toia, Amar Dhanantwari, and Brian Nett. A review of deep learning ct reconstruction: concepts, limitations, and promise in clinical practice. *Current Radiology Reports*, 10(9):101–115, 2022.

Zhou Wang, Alan C Bovik, Hamid R Sheikh, and Eero P Simoncelli. Image quality assessment: from error visibility to structural similarity. *IEEE transactions on image processing*, 13(4):600–612, 2004.

Wenjun Xia, Wenxiang Cong, and Ge Wang. Patch-based denoising diffusion probabilistic model for sparse-view ct reconstruction. *arXiv preprint arXiv:2211.10388*, 2022.

Kai Xu, Shiyu Lu, Bin Huang, Weiwen Wu, and Qiegen Liu. Stage-by-stage wavelet optimization refinement diffusion model for sparse-view ct reconstruction. *IEEE Transactions on Medical Imaging*, 2024.

Guang Yang, Simiao Yu, Hao Dong, Greg Slabaugh, Pier Luigi Dragotti, Xujiong Ye, Fangde Liu, Simon Arridge, Jennifer Keegan, Yike Guo, et al. Dagan: deep de-aliasing generative adversarial networks for fast compressed sensing mri reconstruction. *IEEE transactions on medical imaging*, 37(6):1310–1321, 2017.

Liutao Yang, Rongjun Ge, Shichang Feng, and Daoqiang Zhang. Learning projection views for sparse-view ct reconstruction. In *Proceedings of the 30th ACM International Conference on Multimedia*, pp. 2645–2653, 2022.

Qingsong Yang, Pingkun Yan, Yanbo Zhang, Hengyong Yu, Yongyi Shi, Xuanqin Mou, Mannudeep K Kalra, Yi Zhang, Ling Sun, and Ge Wang. Low dose ct image denoising using a generative adversarial network with wasserstein distance and perceptual loss. *IEEE transactions on medical imaging*, 37(6):1348, 2018.

Ruyi Zha, Tao Jun Lin, Yuanhao Cai, Jiwen Cao, Yanhao Zhang, and Hongdong Li. R^2-gaussian: Rectifying radiative gaussian splatting for tomographic reconstruction. In *Advances in Neural Information Processing Systems (NeurIPS)*, 2024.

Bo Zhu, Jeremiah Z Liu, Stephen F Cauley, Bruce R Rosen, and Matthew S Rosen. Image reconstruction by domain-transform manifold learning. *Nature*, 555(7697):487–492, 2018.

Appendix

A EVALUATION METRICS

In this section, we describe the evaluation metrics used in the paper.

A.1 PEAK SIGNAL-TO-NOISE RATIO (PSNR)

The PSNR (Hore & Ziou, 2010) is a widely used metric to evaluate the quality of the reconstructed images. It is defined as:

$$\text{PSNR}(x, y) = 10 \cdot \log_{10} \left(\frac{\text{MAX}^2}{\text{MSE}(x, y)} \right), \tag{13}$$

where MAX is the maximum possible pixel value of the image and $\text{MSE}(x, y)$ is the mean squared error between the original and reconstructed images.

A.2 STRUCTURAL SIMILARITY INDEX (SSIM)

The SSIM (Wang et al., 2004) is a metric that measures the similarity between two images. It is defined as:

$$\text{SSIM}(x, y) = \frac{(2\mu_x\mu_y + C_1)(2\sigma_{xy} + C_2)}{(\mu_x^2 + \mu_y^2 + C_1)(\sigma_x^2 + \sigma_y^2 + C_2)}, \tag{14}$$

where μ_x and μ_y are the mean values of the images x and y, σ_x^2 and σ_y^2 are the variances of the images, σ_{xy} is the covariance of the images, and C_1 and C_2 are constants to stabilize the division with weak denominator.

B THREE-SIGMA RULE

The *Three-Sigma rule* states that approximately 99.73% of the data in a Gaussian distribution lies within three standard deviations of the mean. This result is derived from the properties of the Gaussian (normal) distribution.

For a random variable X that follows a Gaussian distribution with mean μ and standard deviation σ, the probability density function (PDF) is given by:

$$f(x) = \frac{1}{\sigma\sqrt{2\pi}} \exp\left(-\frac{(x-\mu)^2}{2\sigma^2} \right)$$

To find the probability that X lies within three standard deviations of the mean, i.e., within the interval $[\mu - 3\sigma, \mu + 3\sigma]$, we compute the following probability:

$$P(\mu - 3\sigma \leq X \leq \mu + 3\sigma) = \int_{\mu-3\sigma}^{\mu+3\sigma} \frac{1}{\sigma\sqrt{2\pi}} \exp\left(-\frac{(x-\mu)^2}{2\sigma^2} \right) dx$$

To simplify the integral, we standardize the normal distribution by defining a standard normal variable z as:

$$z = \frac{x - \mu}{\sigma}$$

This transforms the limits of the integral from $[\mu - 3\sigma, \mu + 3\sigma]$ to $[-3, 3]$. The PDF of the standard normal distribution is then:

$$f(z) = \frac{1}{\sqrt{2\pi}} \exp\left(-\frac{z^2}{2} \right)$$

Table 7: Different Types of Medical Image Reconstruction Methods.

	Representative Methods	Full	Sparse	Trainable	Data Indep.	Inf. Speed
Traditional	FBP (Bracewell & Riddle, 1967)	✓	×	×	✓	Real-Time
	IFFT (Gallagher et al., 2008)	✓	✓	×	✓	Real-Time
Direct Learning	AUTOMAP (Zhu et al., 2018)	✓	✓	✓	×	Very Fast
	iRadonMAP (He et al., 2020)	✓	✓	✓	×	Very Fast
Image-Based Denoising	FBPConvNet (Jin et al., 2017)	✓	✓	✓	×	Very Fast
	REDCNN (Chen et al., 2017)	✓	✓	✓	×	Very Fast
Dual-Domain Reconstruction	HDNet (Hu et al., 2020)	✓	✓	✓	×	Very Fast
Diffusion-Based DLR	MCG (Chung et al., 2022)	✓	✓	✓	×	Low
	DiffusionMBIR (Chung et al., 2023)	✓	✓	✓	×	Low
	SWORD (Xu et al., 2024)	✓	✓	✓	×	Low
3D Scene Reconstruction	NeRP (Shen et al., 2022)	✓	✓	✓	✓	Medium
	DIFGaussian (Lin et al., 2024)	✓	✓	✓	✓	Fast
	3DGR-CAR (Fu et al., 2024)	✓	✓	✓	✓	Fast
	X-Gaussian (Lin et al., 2024)	✓	✓	✓	✓	Fast
	R^2-Gaussian (Zha et al., 2024)	✓	✓	✓	✓	Fast
Our method	GBIR	✓	✓	✓	✓	Fast

Thus, the probability becomes:

$$P(-3 \leq z \leq 3) = \int_{-3}^{3} \frac{1}{\sqrt{2\pi}} \exp\left(-\frac{z^2}{2}\right) dz$$

This integral does not have a closed-form solution but can be numerically approximated. Using standard numerical methods or precomputed values from the cumulative distribution function (CDF) of the standard normal distribution, the result of this integral is approximately:

$$P(-3 \leq z \leq 3) \approx 0.9973$$

This confirms that approximately 99.73% of the data in a Gaussian distribution lies within three standard deviations from the mean.

The contribution of a Gaussian distribution decreases rapidly as the distance from its mean increases. Therefore, in medical image reconstruction, truncating the Gaussian distribution at three standard deviations from the mean can remove the negligible tail values while retaining the majority of the distribution.

C VISUALIZATION

Figure 5 shows the gradual convergence of the GBIR framework for a brain CT reconstruction. The 3D volume is gradually reconstructed from the initial random noise to the final clear structure. The convergence process is conducted in an end-to-end manner, and the final 3D volume is obtained after convergence.

D DATA ACQUISITION AND PROCESSING

Staff Configuration All CT and MRI scans were collected and evaluated by three experienced radiologists. The radiologists were responsible for reviewing the scans and identifying any abnormalities or diseases. Among the three radiologists, two were senior radiologists with over 10 years of experience, and one was a junior radiologist with 5 years of experience. The radiologists worked together to ensure the accuracy and consistency of the data.

Data Selection The CT and MRI scans were selected based on the following criteria: (1) the scans were of high quality, with minimal artifacts or noise, (2) the scans covered a wide range of body parts and conditions, and (3) the scans were representative of the clinical cases encountered in practice.

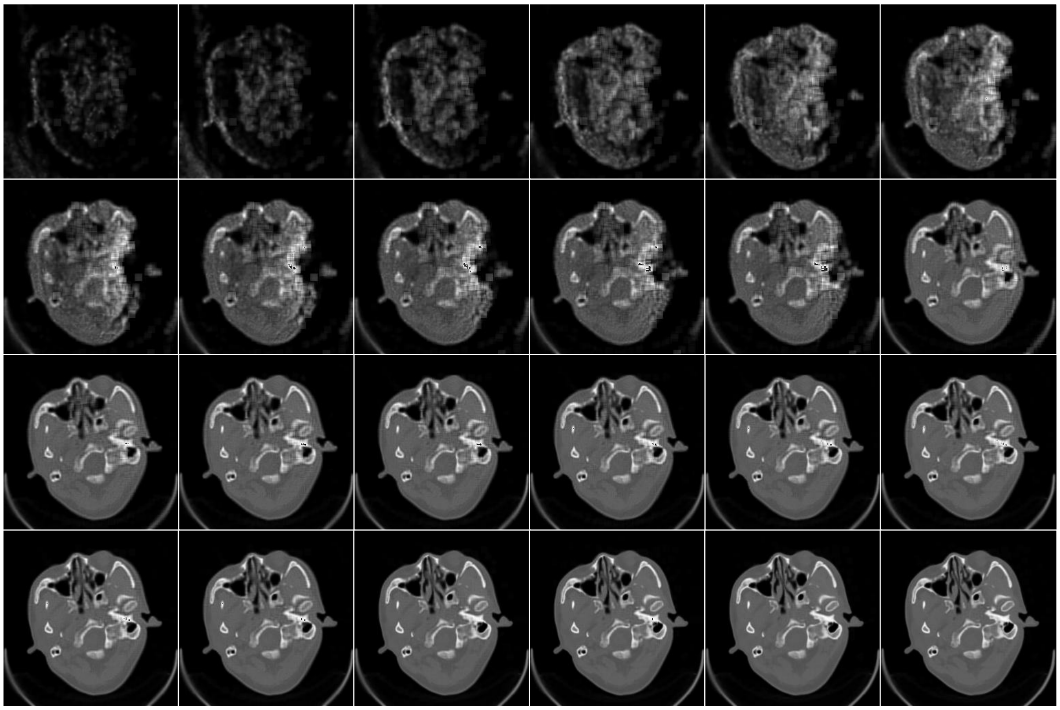

Figure 5: Iterative reconstruction visualization of our GBIR.

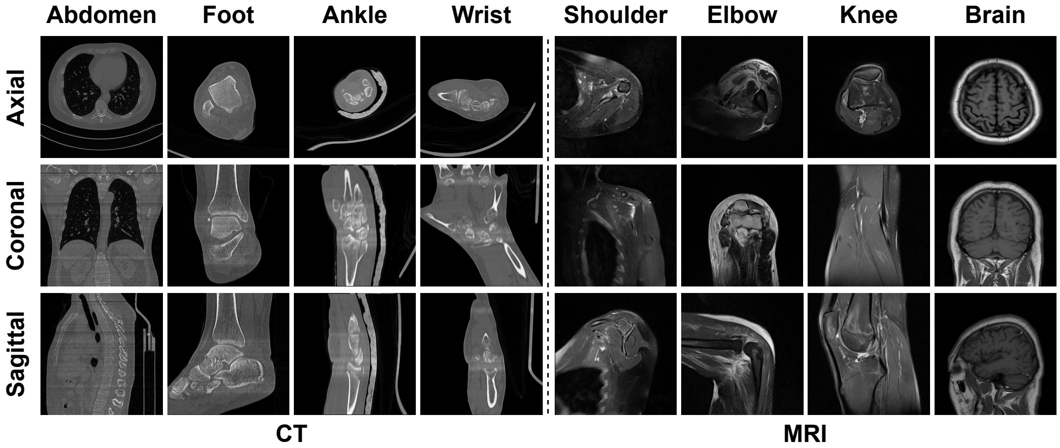

Figure 6: Examples of MORE dataset, containing CT and MRI scans from 4 different organs.

In practice, the radiologists first categorized the scans based on the body part imaged and the condition depicted, and then select typical cases from the corresponding parts, including internal and external medicine and acute and chronic cases.

Scan Parameters Each individual sample selects the window width and window position that are commonly displayed for the corresponding disease type. Samples of two slice thicknesses (1mm and 3mm) are chosen for CT scans, and two echo times (TE) are chosen for MRI scans. The MRI scans are collected using a 1.5T MRI scanner.

Data processing The image data is provided and easy to use. Slices within the same sequence can be identified with file names, and each slice is stored as a 2D array of pixel intensities without extra transformation. Intensity values depend on the type of scan (CT or MRI) and the scanning

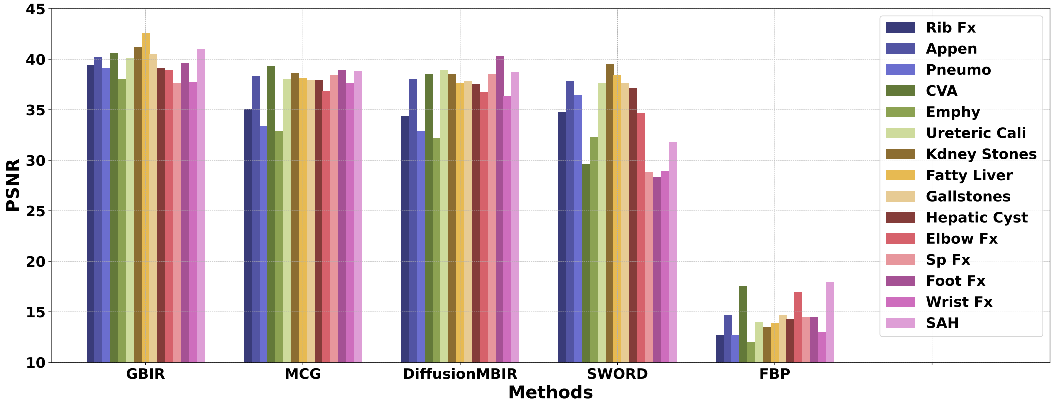

Figure 7: Performance of various methods on different organs within our MORE dataset, evaluated by the PSNR metric on 60 view SV-CT.

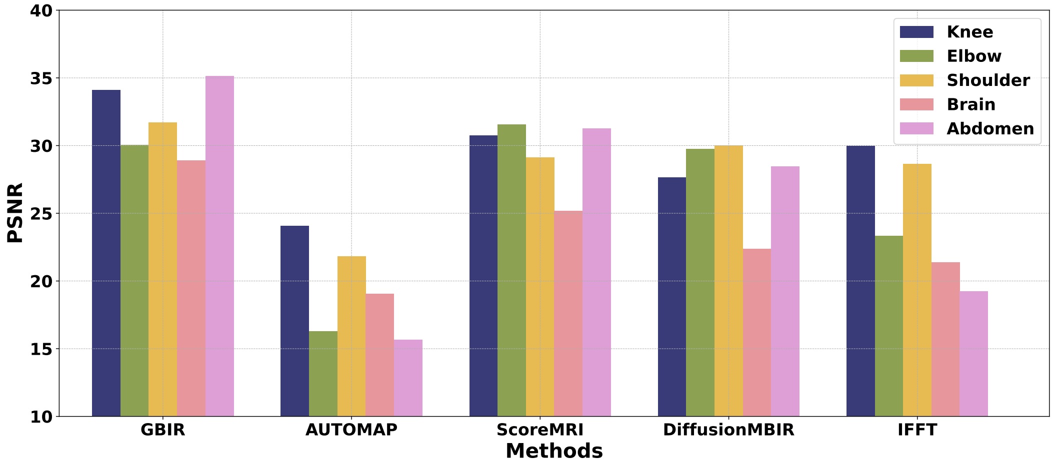

Figure 8: Performance of various methods on different organs within our MORE dataset, evaluated by the PSNR metric on axial CS-MRI.

parameters. For CT scans, the pixel intensities represent Hounsfield units, while for MRI scans, the pixel intensities represent signal intensities. To facilitate other researchers' use, we also provide PNG images for each DICOM file which can be easily visualized.

Table 8: SV-CT reconstruction of MORE dataset **Subarachnoid Hemorrhage** trained on AAPM-Mayo LDCT Dataset. Best in **Bold.**

Method	Extra Data	180-view		120-view		90-view		60-view	
		PSNR	SSIM	PSNR	SSIM	PSNR	SSIM	PSNR	SSIM
RED-CNN (Chen et al., 2017)	✓	28.03	0.818	27.76	0.795	27.43	0.792	26.40	0.787
MCG (Chung et al., 2022)	✓	35.85	0.874	35.90	0.875	35.78	0.870	35.59	0.869
DiffusionMBIR (Chung et al., 2023)	✓	36.65	0.962	36.59	0.962	36.57	0.963	36.02	0.961
SWORD (Xu et al., 2024)	✓	38.03	0.971	37.36	0.954	32.42	0.885	28.83	0.813
FBP (Bracewell & Riddle, 1967)	×	21.31	0.440	20.84	0.423	19.22	0.404	17.93	0.361
NeRP (Shen et al., 2022)	×	23.72	0.760	23.34	0.760	23.84	0.800	24.04	0.791
GBIR (Ours)	×	**43.29**	**0.993**	**42.74**	**0.993**	**41.98**	**0.992**	**41.02**	**0.992**

Table 9: SV-CT reconstruction on **Emphysema**. Best in **Bold.**

Method	Extra Data	180-view		120-view		90-view		60-view	
		PSNR	SSIM	PSNR	SSIM	PSNR	SSIM	PSNR	SSIM
RED-CNN (Chen et al., 2017)	✓	29.58	0.714	28.44	0.644	27.06	0.623	27.27	0.588
MCG (Chung et al., 2022)	✓	32.72	0.820	32.84	0.821	34.47	0.843	32.90	0.820
DiffusionMBIR (Chung et al., 2023)	✓	32.58	0.933	32.64	0.936	32.45	0.932	32.24	0.932
SWORD (Xu et al., 2024)	✓	35.38	0.879	34.52	0.864	33.78	0.849	32.30	0.827
FBP (Bracewell & Riddle, 1967)	×	18.55	0.365	16.29	0.293	14.77	0.248	12.03	0.193
NeRP (Shen et al., 2022)	×	25.41	0.744	25.21	0.735	25.40	0.745	25.39	0.745
GBIR (Ours)	×	**39.47**	**0.950**	**39.04**	**0.946**	**38.42**	**0.941**	**38.04**	**0.937**

Table 10: SV-CT reconstruction on **Ureteral Calculi**. Best in **Bold.**

Method	Extra Data	180-view		120-view		90-view		60-view	
		PSNR	SSIM	PSNR	SSIM	PSNR	SSIM	PSNR	SSIM
RED-CNN (Chen et al., 2017)	✓	37.04	0.901	35.63	0.913	32.07	0.759	31.46	0.844
MCG (Chung et al., 2022)	✓	37.94	0.901	37.99	0.901	38.04	0.902	38.05	0.902
DiffusionMBIR (Chung et al., 2023)	✓	38.37	0.968	38.24	0.967	38.13	0.967	38.90	0.966
SWORD (Xu et al., 2024)	✓	42.35	0.973	40.93	0.967	39.42	0.960	37.63	0.947
FBP (Bracewell & Riddle, 1967)	×	23.09	0.515	19.42	0.462	16.89	0.416	14.02	0.355
NeRP (Shen et al., 2022)	×	26.91	0.801	26.68	0.789	26.95	0.802	26.66	0.785
GBIR (Ours)	×	**43.43**	**0.982**	**42.24**	**0.980**	**40.82**	**0.976**	**40.11**	**0.975**

Table 11: SV-CT reconstruction on **Rib Fracture**. Best in **Bold.**

Method	Extra Data	180-view		120-view		90-view		60-view	
		PSNR	SSIM	PSNR	SSIM	PSNR	SSIM	PSNR	SSIM
RED-CNN (Chen et al., 2017)	✓	29.61	0.707	28.97	0.682	27.94	0.658	27.97	0.585
MCG (Chung et al., 2022)	✓	34.81	0.851	34.94	0.852	34.96	0.853	35.07	0.854
DiffusionMBIR (Chung et al., 2023)	✓	34.64	0.950	34.64	0.952	34.54	0,951	34.35	**0.950**
SWORD (Xu et al., 2024)	✓	36.51	0.877	35.90	0.864	35.53	0.855	34.76	0.838
FBP (Bracewell & Riddle, 1967)	×	19.33	0.388	16.64	0.324	14.76	0.280	12.69	0.230
NeRP (Shen et al., 2022)	×	25.77	0.778	25.10	0.744	25.63	0.771	25.60	0.769
GBIR (Ours)	×	**42.43**	**0.972**	**41.05**	**0.962**	**40.01**	**0.953**	**39.43**	0.948

Table 12: SV-CT reconstruction on **Appendicitis**. Best in **Bold.**

Method	Extra Data	180-view		120-view		90-view		60-view	
		PSNR	SSIM	PSNR	SSIM	PSNR	SSIM	PSNR	SSIM
RED-CNN (Chen et al., 2017)	✓	36.96	0.904	35.54	0.906	31.30	0.838	32.59	0.854
MCG (Chung et al., 2022)	✓	38.76	0.908	38.96	0.909	38.97	0.897	38.36	0.899
DiffusionMBIR (Chung et al., 2023)	✓	38.34	0.960	38.28	0.959	38.24	0.966	38.00	0.967
SWORD (Xu et al., 2024)	✓	**44.18**	0.976	**42.62**	0.971	40.85	0.964	37.79	0.949
FBP (Bracewell & Riddle, 1967)	×	23.37	0.516	19.63	0.462	18.17	0.427	14.67	0.366
NeRP (Shen et al., 2022)	×	27.15	0.821	27.25	0.817	27.38	0.819	27.28	0.817
GBIR (Ours)	×	42.03	**0.981**	41.63	**0.981**	**41.15**	**0.979**	**40.22**	**0.976**

Table 13: SV-CT reconstruction on **Pneumonia**. Best in **Bold.**

Method	Extra Data	180-view		120-view		90-view		60-view	
		PSNR	SSIM	PSNR	SSIM	PSNR	SSIM	PSNR	SSIM
RED-CNN (Chen et al., 2017)	✓	31.78	0.733	30.43	0.672	29.22	0.680	27.82	0.578
MCG (Chung et al., 2022)	✓	32.87	0.810	33.05	0.813	33.19	0.814	33.33	0.815
DiffusionMBIR (Chung et al., 2023)	✓	33.34	0.954	33.26	0.953	33.10	0.952	32.86	**0.951**
SWORD (Xu et al., 2024)	✓	39.69	0.901	38.75	0.887	38.02	0.875	36.40	0.850
FBP (Bracewell & Riddle, 1967)	×	17.57	0.323	15.73	0.264	14.66	0.229	12.73	0.182
NeRP (Shen et al., 2022)	×	25.52	0.694	26.16	0.733	25.93	0.722	25.64	0.701
GBIR (Ours)	×	**41.77**	**0.967**	**40.96**	**0.962**	**40.31**	**0.956**	**39.11**	0.946

Table 14: SV-CT reconstruction on **Cerebral Hemorrhage**. Best in **Bold.**

Method	Extra Data	180-view		120-view		90-view		60-view	
		PSNR	SSIM	PSNR	SSIM	PSNR	SSIM	PSNR	SSIM
RED-CNN (Chen et al., 2017)	✓	35.47	0.895	33.29	0.864	30.46	0.786	29.26	0.766
MCG (Chung et al., 2022)	✓	39.14	0.898	39.23	0.899	39.32	0.899	39.31	0.899
DiffusionMBIR (Chung et al., 2023)	✓	39.04	0.969	39.29	0.973	39.05	0.971	38.53	0.969
SWORD (Xu et al., 2024)	✓	34.90	0.742	33.50	0.740	31.86	0.737	29.57	0.732
FBP (Bracewell & Riddle, 1967)	×	24.13	0.526	21.54	0.490	19.70	0.460	17.52	0.413
NeRP (Shen et al., 2022)	×	25.38	0.789	25.98	0.804	25.02	0.760	24.23	0.764
GBIR (Ours)	×	**43.71**	**0.984**	**42.94**	**0.981**	**41.68**	**0.978**	**40.56**	**0.974**

Table 15: SV-CT reconstruction on **Kidney Stones**. Best in **Bold.**

Method	Extra Data	180-view		120-view		90-view		60-view	
		PSNR	SSIM	PSNR	SSIM	PSNR	SSIM	PSNR	SSIM
RED-CNN (Chen et al., 2017)	✓	36.65	0.882	34.70	0.909	31.98	0.802	30.89	0.798
MCG (Chung et al., 2022)	✓	38.16	0.909	38.43	0.911	38.49	0.912	38.67	0.913
DiffusionMBIR (Chung et al., 2023)	✓	28.84	0.964	38.92	0.966	38.79	0.964	38.54	0.964
SWORD (Xu et al., 2024)	✓	43.58	0.980	42.27	0.976	40.95	0.971	39.51	0.961
FBP (Bracewell & Riddle, 1967)	×	22.88	0.483	19.39	0.439	16.27	0.398	13.52	0.341
NeRP (Shen et al., 2022)	×	26.17	0.767	26.25	0.773	26.11	0.772	26.16	0.776
GBIR (Ours)	×	**44.37**	**0.988**	**43.45**	**0.987**	**42.99**	**0.986**	**41.20**	**0.982**

Table 16: SV-CT reconstruction on **Fatty Liver**. Best in **Bold.**

Method	Extra Data	180-view		120-view		90-view		60-view	
		PSNR	SSIM	PSNR	SSIM	PSNR	SSIM	PSNR	SSIM
RED-CNN (Chen et al., 2017)	✓	36.60	0.857	35.64	0.876	32.48	0.743	32.73	0.836
MCG (Chung et al., 2022)	✓	37.97	0.897	38.07	0.897	38.12	0.898	38.14	0.898
DiffusionMBIR (Chung et al., 2023)	✓	38.04	0.961	37.95	0.960	37.86	0.960	37.68	0.959
SWORD (Xu et al., 2024)	✓	43.47	0.973	42.21	0.968	40.76	0.961	38.45	0.948
FBP (Bracewell & Riddle, 1967)	×	22.29	0.482	18.10	0.431	16.54	0.395	13.87	0.342
NeRP (Shen et al., 2022)	×	26.89	0.785	27.27	0.808	26.81	0.784	26.93	0.792
GBIR (Ours)	×	**44.46**	**0.987**	**43.96**	**0.986**	**43.47**	**0.985**	**42.54**	**0.983**

Table 17: SV-CT reconstruction on **Gallbladder Stones**. Best in **Bold.**

Method	Extra Data	180-view		120-view		90-view		60-view	
		PSNR	SSIM	PSNR	SSIM	PSNR	SSIM	PSNR	SSIM
RED-CNN (Chen et al., 2017)	✓	36.15	0.892	35.59	0.913	32.41	0.797	31.80	0.868
MCG (Chung et al., 2022)	✓	38.13	0.897	38.47	0.901	38.01	0.897	37.95	0.899
DiffusionMBIR (Chung et al., 2023)	✓	38.20	0.966	38.22	0.966	38.19	0.967	37.86	0.965
SWORD (Xu et al., 2024)	✓	43.66	0.974	42.34	0.969	40.56	0.961	37.64	0.943
FBP (Bracewell & Riddle, 1967)	×	23.94	0.548	20.27	0.494	17.46	0.445	14.68	0.380
NeRP (Shen et al., 2022)	×	27.03	0.809	27.12	0.814	26.81	0.799	26.86	0.806
GBIR (Ours)	×	**43.73**	**0.985**	**42.91**	**0.984**	**42.15**	**0.982**	**40.55**	**0.977**

Table 18: SV-CT reconstruction on **Hepatic Cyst**. Best in **Bold.**

Method	Extra Data	180-view		120-view		90-view		60-view	
		PSNR	SSIM	PSNR	SSIM	PSNR	SSIM	PSNR	SSIM
RED-CNN (Chen et al., 2017)	✓	36.74	0.930	35.52	0.905	31.33	0.791	33.36	0.854
MCG (Chung et al., 2022)	✓	37.87	0.891	37.91	0.891	37.94	0.891	37.94	0.891
DiffusionMBIR (Chung et al., 2023)	✓	37.92	0.955	38.02	0.957	37.91	0.956	37.50	0.952
SWORD (Xu et al., 2024)	✓	42.84	0.973	41.42	0.967	39.81	0.960	37.12	0.946
FBP (Bracewell & Riddle, 1967)	×	25.26	0.603	19.94	0.525	17.27	0.475	14.26	0.416
NeRP (Shen et al., 2022)	×	26.65	0.808	26.57	0.804	26.65	0.808	26.39	0.799
GBIR (Ours)	×	**42.96**	**0.981**	**42.29**	**0.980**	**41.47**	**0.977**	**39.12**	**0.971**

Table 19: SV-CT reconstruction on **Elbow Fracture**. Best in **Bold.**

Method	Extra Data	180-view		120-view		90-view		60-view	
		PSNR	SSIM	PSNR	SSIM	PSNR	SSIM	PSNR	SSIM
RED-CNN (Chen et al., 2017)	✓	34.41	0.847	34.05	0.789	27.42	0.777	29.82	0.732
MCG (Chung et al., 2022)	✓	37.20	0.857	37.13	0.858	37.08	0.856	36.80	0.852
DiffusionMBIR (Chung et al., 2023)	✓	37.06	0.932	36.93	0.930	36.89	0.931	36.75	0.930
SWORD (Xu et al., 2024)	✓	**42.83**	0.959	38.67	0.917	37.39	0.901	34.71	0.865
FBP (Bracewell & Riddle, 1967)	×	26.15	0.459	22.32	0.382	19.93	0.337	16.95	0.279
NeRP (Shen et al., 2022)	×	28.14	0.826	28.31	0.827	28.06	0.823	28.18	0.835
GBIR (Ours)	×	42.82	**0.961**	**41.94**	**0.954**	**41.19**	**0.949**	**38.97**	**0.978**

Table 20: SV-CT reconstruction on **Spinal Fracture**. Best in **Bold.**

Method	Extra Data	180-view		120-view		90-view		60-view	
		PSNR	SSIM	PSNR	SSIM	PSNR	SSIM	PSNR	SSIM
RED-CNN (Chen et al., 2017)	✓	23.86	0.866	23.94	0.841	23.92	0.832	23.70	0.810
MCG (Chung et al., 2022)	✓	38.52	0.913	38.52	0.913	38.48	0.912	38.40	0.911
DiffusionMBIR (Chung et al., 2023)	✓	39.34	0.973	39.27	0.973	**39.08**	**0.972**	**38.49**	**0.969**
SWORD (Xu et al., 2024)	✓	40.94	0.946	38.02	0.930	34.68	0.901	28.85	0.834
FBP (Bracewell & Riddle, 1967)	×	16.41	0.793	15.20	0.766	14.73	0.741	13.96	0.698
NeRP (Shen et al., 2022)	×	28.10	0.847	26.24	0.779	27.95	0.840	26.48	0.790
GBIR (Ours)	×	**41.23**	**0.981**	**39.70**	**0.977**	38.41	0.971	37.68	0.968

Table 21: SV-CT reconstruction on **Foot Fracture**. Best in **Bold.**

Method	Extra Data	180-view		120-view		90-view		60-view	
		PSNR	SSIM	PSNR	SSIM	PSNR	SSIM	PSNR	SSIM
RED-CNN (Chen et al., 2017)	✓	37.53	0.860	35.61	0.783	32.52	0.817	32.46	0.837
MCG (Chung et al., 2022)	✓	39.40	0.891	39.62	0.895	39.43	0.894	39.45	0.894
DiffusionMBIR (Chung et al., 2023)	✓	40.45	0.956	40.31	0.955	40.22	0.954	**40.26**	0.957
SWORD (Xu et al., 2024)	✓	34.92	0.927	36.40	0.905	31.95	0.866	28.33	0.783
FBP (Bracewell & Riddle, 1967)	×	23.45	0.235	18.80	0.181	17.23	0.160	14.46	0.132
NeRP (Shen et al., 2022)	×	30.69	0.921	30.82	0.926	30.76	0.932	30.56	0.927
GBIR (Ours)	×	**41.81**	**0.981**	**41.21**	**0.980**	**40.51**	**0.974**	39.60	**0.977**

Table 22: SV-CT reconstruction on **Wrist Fracture**. Best in **Bold.**

Method	Extra Data	180-view		120-view		90-view		60-view	
		PSNR	SSIM	PSNR	SSIM	PSNR	SSIM	PSNR	SSIM
RED-CNN (Chen et al., 2017)	✓	36.61	0.810	34.73	0.825	31.73	0.870	30.78	0.744
MCG (Chung et al., 2022)	✓	37.14	0.887	37.53	0.889	37.65	0.890	37.64	0.889
DiffusionMBIR (Chung et al., 2023)	✓	36.91	0.953	36.94	0.954	36.73	0.952	36.31	0.950
SWORD (Xu et al., 2024)	✓	36.74	0.903	33.91	0.874	31.57	0.832	28.91	0.766
FBP (Bracewell & Riddle, 1967)	×	21.35	0.231	17.95	0.197	15.69	0.174	12.96	0.146
NeRP (Shen et al., 2022)	×	29.55	0.893	28.77	0.891	29.62	0.897	29.56	0.893
GBIR (Ours)	×	**40.28**	**0.984**	**39.71**	**0.983**	**38.89**	**0.976**	**37.78**	**0.973**

Table 23: SV-CT reconstruction on **Subarachnoid Hemorrhage**. Best in **Bold.**

Method	Extra Data	180-view		120-view		90-view		60-view	
		PSNR	SSIM	PSNR	SSIM	PSNR	SSIM	PSNR	SSIM
RED-CNN (Chen et al., 2017)	✓	29.52	0.874	29.65	0.877	29.55	0.877	29.42	0.863
MCG (Chung et al., 2022)	✓	38.78	0.908	38.87	0.909	38.81	0.908	38.79	0.908
DiffusionMBIR (Chung et al., 2023)	✓	39.46	0.975	39.38	0.975	39.20	0.974	38.70	0.973
SWORD (Xu et al., 2024)	✓	42.54	0.965	39.60	0.955	36.71	0.938	31.84	0.895
FBP (Bracewell & Riddle, 1967)	×	21.31	0.440	20.84	0.423	19.22	0.404	17.93	0.361
NeRP (Shen et al., 2022)	×	23.72	0.760	23.34	0.760	23.84	0.800	24.04	0.791
GBIR (Ours)	×	**43.29**	**0.993**	**42.74**	**0.993**	**41.98**	**0.992**	**41.02**	**0.992**

Table 24: CS-MRI reconstruction on **Brain**. Best in **Bold.**

Method	Extra Data	Axial		Coronal		Sagittal	
		PSNR	SSIM	PSNR	SSIM	PSNR	SSIM
RED-CNN (Chen et al., 2017)	✓	26.36	0.686	29.49	0.786	29.05	0.731
AUTOMAP (Zhu et al., 2018)	✓	19.06	0.635	17.75	0.593	17.58	0.489
ScoreMRI (Chung & Ye, 2022)	✓	25.17	0.725	**32.46**	0.786	28.99	0.763
DiffusionMBIR (Chung et al., 2023)	✓	22.37	0.703	26.13	0.694	**29.13**	0.784
IFFT (Gallagher et al., 2008)	×	21.39	0.711	20.60	0.750	20.96	0.726
GBIR (Ours)	×	**28.89**	**0.895**	29.21	**0.914**	29.07	**0.937**

Table 25: CS-MRI reconstruction on **Abdomen**. Best in **Bold.**

Method	Extra Data	Axial		Coronal		Sagittal	
		PSNR	SSIM	PSNR	SSIM	PSNR	SSIM
RED-CNN (Chen et al., 2017)	✓	33.63	0.858	31.48	0.847	31.39	0.671
AUTOMAP (Zhu et al., 2018)	✓	15.64	0.514	17.20	0.516	17.61	0.397
ScoreMRI (Chung & Ye, 2022)	✓	31.26	0.789	31.34	0.839	28.09	0.604
DiffusionMBIR (Chung et al., 2023)	✓	28.45	0.731	21.72	0.793	25.69	0.654
IFFT (Gallagher et al., 2008)	×	19.23	0.718	19.93	0.750	22.29	0.665
GBIR (Ours)	×	**35.15**	**0.935**	**33.29**	**0.922**	**34.86**	**0.955**

Table 26: CS-MRI reconstruction on **Shoulder**. Best in **Bold.**

Method	Extra Data	Axial		Coronal		Sagittal	
		PSNR	SSIM	PSNR	SSIM	PSNR	SSIM
RED-CNN (Chen et al., 2017)	✓	27.95	0.724	27.41	0.769	29.64	0.746
AUTOMAP (Zhu et al., 2018)	✓	21.81	0.657	23.83	0.622	21.18	0.663
ScoreMRI (Chung & Ye, 2022)	✓	29.12	0.763	30.89	**0.873**	30.55	0.814
DiffusionMBIR (Chung et al., 2023)	✓	30.01	**0.781**	27.90	0.788	30.74	0.863
IFFT (Gallagher et al., 2008)	×	28.66	0.733	27.49	0.693	28.83	0.745
GBIR (Ours)	×	**32.64**	0.730	**31.71**	0.868	**33.54**	**0.919**

Table 27: CS-MRI reconstruction on **Knee**. Best in **Bold.**

Method	Extra Data	Axial		Coronal		Sagittal	
		PSNR	SSIM	PSNR	SSIM	PSNR	SSIM
RED-CNN (Chen et al., 2017)	✓	32.98	0.786	30.29	**0.862**	27.86	0.822
AUTOMAP (Zhu et al., 2018)	✓	24.07	0.818	22.31	0.667	18.22	0.654
ScoreMRI (Chung & Ye, 2022)	✓	30.75	0.623	**33.18**	0.847	**31.46**	0.780
DiffusionMBIR (Chung et al., 2023)	✓	27.63	0.617	29.46	0.813	23.94	0.760
IFFT (Gallagher et al., 2008)	×	29.98	**0.827**	26.30	0.790	20.48	0.713
GBIR (Ours)	×	**34.11**	0.753	29.70	0.826	27.13	**0.857**

Table 28: CS-MRI reconstruction on **Elbow**. Best in **Bold.**

Method	Extra Data	Axial		Coronal		Sagittal	
		PSNR	SSIM	PSNR	SSIM	PSNR	SSIM
RED-CNN (Chen et al., 2017)	✓	27.17	**0.846**	30.34	0.673	27.63	0.810
AUTOMAP (Zhu et al., 2018)	✓	16.30	0.521	20.97	0.701	16.23	0.458
ScoreMRI (Chung & Ye, 2022)	✓	**31.54**	0.814	29.58	0.580	28.72	0.813
DiffusionMBIR (Chung et al., 2023)	✓	29.76	0.823	30.11	0.732	29.45	0.798
IFFT (Gallagher et al., 2008)	×	23.34	0.810	22.86	0.662	23.14	0.771
GBIR (Ours)	×	30.05	0.812	**31.08**	**0.878**	**29.96**	**0.897**